Physica Medica 120 (2024) 103337

Contents lists available at ScienceDirect

Physica Medica

journal homepage: www.elsevier.com/locate/ejmp

Original paper

# Assessment of temporal resolution and detectability of moving objects in CT: A task-based image quality study

P. Monnin [a,*], D. Rotzinger [b], A. Viry [a], V. Vitzthum [a], D. Racine [a]

[a] Institute of Radiation Physics (IRA), Lausanne University Hospital (CHUV) and University of Lausanne (UNIL), Rue du Grand-Pré 1, 1007 Lausanne, Switzerland
[b] Department of Diagnostic and Interventional Radiology, Lausanne University Hospital (CHUV) and University of Lausanne (UNIL), Rue du Bugnon 46, 1011 Lausanne, Switzerland

ARTICLE INFO

*Keywords:*
Computed tomography
Image quality
Temporal resolution
Detectability index

ABSTRACT

The metrics used for assessing image quality in computed tomography (CT) do not integrate the influence of temporal resolution. A shortcoming in the assessment of image quality for imaging protocols where motion blur can therefore occur. We developed a method to calculate the temporal resolution of standard CT protocols and introduced a specific spatiotemporal formulation of the non-prewhitening with eye filter (NPWE) model observer to assess the detectability of moving objects as a function of their speed. We scanned a cubic water phantom with a plexiglass cylindrical insert (120 HU) using a large panel of acquisition parameters (rotation times, pitch factors and collimation widths) on two systems (GE Revolution Apex and Siemens SOMATOM Force) to determine the in-plane task-based transfer functions (TTF) and noise power spectra (NPS). The phantom set in a uniform rectilinear motion in the transverse plane allowed the temporal modulation transfer function (MTF) calculation. The temporal MTF appropriately compared the temporal resolution of the various acquisition protocols. The longitudinal TTF was measured using a thin tungsten wire. The detectability index showed the advantage of applying high rotation speed, wide collimations and high pitch for object detection in the presence of motion. No counterpart to the increase in these three parameters was found in the in-plane and longitudinal image quality.

## 1. Introduction

In medical imaging, one of the key factors affecting image quality is temporal resolution, which refers to the time needed to acquire an image during a dynamic process. High temporal resolution in CT acquisition is crucial for reducing motion artifacts and improving image quality, especially for patients unable to hold their breath, or have aortic pulsation and cardiac-related pulmonary parenchyma motion artifacts [1,2]. The temporal resolution of CT is determined by factors such as gantry rotation time, helical pitch factor and collimation width [3].

Advances in CT technology have allowed the decrease in rotation time, the use of higher pitch factors and wide collimations without suffering from under-sampling issues. Traditionally, an optimal longitudinal resolution required data overlap obtained at low pitch, but current CT systems provide adequate longitudinal resolution even for pitch factors larger than 1.0 [4]. Significant reductions in acquisition time, a major reduction of motion blur and artifacts were achieved [5,6,7]. Another advancement towards high temporal resolution came with the introduction of partial-scan reconstruction in cardiac CT [8]. Dual-source CT brought another notable improvement in reducing the acquisition time by a factor two [9,10]. The combination of high-pitch with dual-source can provide data combining sufficient volumetric and temporal resolutions [11,12].

Several methods have been developed to measure temporal resolution in CT, including the temporal sensitivity profile (TSP) introduced by Tagushi and Anno in 2000 [13]. This function characterizes the temporal resolution equivalent to the slice sensitivity profile for the longitudinal resolution. More recently, McCollough *et al* [14] developed a method where the angular extent of ring artifact created by the rotation of a punctual object provided an indication of the time used to generate an image. Ichikawa *et al* [15] and Hara *et al* [16] used the motion of a small metallic ball to generate the spatiotemporal signal needed to determine the FWHM of the TSP. Calculating the temporal modulation transfer function (MTF) using the Fourier transform of the TSP generated by a moving target paved the way to measuring the temporal performance of CT acquisition beyond the characterization of an artifact [17,18]. The temporal MTF can be used in model observers to assess spatiotemporal task-based image quality that accounts for and quantifies

* Corresponding author.
*E-mail address:* pascal.monnin@chuv.ch (P. Monnin).

https://doi.org/10.1016/j.ejmp.2024.103337
Received 2 May 2023; Received in revised form 12 March 2024; Accepted 25 March 2024
Available online 28 March 2024

**Table 1**
Imaging protocols for the GE Revolution Apex system.

| Protocol | Tube potential (kV) | Rotation time (s) | Current (fixed) (mA) | Pitch factor | Collimation (mm) | Phantom speed (mm/s) |
|---|---|---|---|---|---|---|
| 1 | 120 | 0.23 | 300 | 0.984 | 64 x 0.625 | 14.0 |
| 2 | 120 | 0.28 | 245 | 0.984 | 64 x 0.625 | 12.0 |
| 3 | 120 | 0.35 | 195 | 0.984 | 64 x 0.625 | 9.0 |
| 4 | 120 | 0.50 | 135 | 0.984 | 64 x 0.625 | 7.0 |
| 5 | 120 | 0.70 | 100 | 0.984 | 64 x 0.625 | 5.0 |
| 6 | 120 | 1.00 | 70 | 0.984 | 64 x 0.625 | 3.0 |
| 7 | 120 | 0.28 | 130 | 0.516 | 64 x 0.625 | 6.0 |
| 8 | 120 | 0.28 | 345 | 1.375 | 64 x 0.625 | 16.0 |
| 9 | 120 | 0.28 | 380 | 1.531 | 64 x 0.625 | 18.0 |
| 10 | 120 | 0.28 | 385 | 0.984 | 128 x 0.625 | 23.0 |

**Table 2**
Imaging protocols for the Siemens SOMATOM Force system.

| Protocol | Tube potential (kV) | Rotation time (s) | Effective mAs | Pitch factor | Collimation (mm) | Phantom speed (mm/s) |
|---|---|---|---|---|---|---|
| 1 | 120 | 0.25 | 75 | 1.0 | 48 x 1.2 | 16.0 |
| 2 | 120 | 0.50 | 75 | 1.0 | 48 x 1.2 | 8.0 |
| 3 | 120 | 1.00 | 75 | 1.0 | 48 x 1.2 | 4.0 |
| 4 | 120 | 0.25 | 75 | 0.35 | 48 x 1.2 | 6.0 |
| 5 | 120 | 0.25 | 75 | 0.50 | 48 x 1.2 | 8.0 |
| 6 | 120 | 0.25 | 75 | 1.2 | 48 x 1.2 | 19.0 |
| 7 | 120 | 0.25 | 75 | 1.5 | 48 x 1.2 | 24.0 |
| 8 | 120 | 0.25 | 75 | 1.0 | 64 x 0.6 | 11.0 |
| 9 | 120 | 0.25 | 75 | 1.0 | 192 x 0.6 | 32.0 |
| 10* | 120 | 0.25 | 75 | 3.2 | 192 x 0.6 | 46.0 |

*High-pitch dual-source protocol.

the effect of object motion on detectability. These models can be used in the framework of the optimization of spatiotemporal parameters of CT protocols which require high image quality and high temporal resolution.

In this work, we propose a methodology to assess the temporal MTF at low speed, which respects the assumption of a small-signal approach, for various acquisition protocols on two modern CT systems with different rotation times, pitch factors and collimation widths. The validity of the method was tested using variations of basic acquisition parameters: gantry rotation time, collimation width and pitch. The temporal MTF is then used in the NPWE model to evaluate the detectability index of a moving object as a function of the motion speed. This allowed us to assess the trade-offs between temporal resolution and image quality using a task-based model observer assessment [19,20,21]. The method presented in our study allows CT benchmarking which takes into account the loss of detectability due to motion blur characterized as a function of the object speed.

## 2. Material and methods

### 2.1. Data acquisition

To assess the effect of different acquisition parameters on temporal resolution and image quality in CT protocols, we imaged a cubic water phantom with a side of 160 mm containing a 70-mm-diameter central polymethylmethacrylate cylindrical insert (PMMA, average CT number at 120 kVp ≈ 120 HU). The cylindrical insert, 70 mm long, was positioned at the phantom centre, leaving a homogenous water volume around to measure image noise. The study involved two CT systems: a wide-detector GE Revolution Apex (GE Healthcare, Milwaukee, MI) and a dual-source Siemens SOMATOM Force (Siemens Healthcare, Forchheim, Germany). The phantom was fixed on a motorized mobile bench and aligned in the longitudinal direction at the scanner isocentre using the positioning lasers. The phantom moved horizontally on the CT table, parallel to the transverse plane, in a uniform rectilinear motion. The motor was driven by 1000 pulses / rotation with a speed control rate of 2.5 kHz (400 μs). In this study, three parameters were varied: the gantry rotation time, the helical pitch, and the collimation width. Their effect on the temporal resolution and image quality of the CT protocols was measured. Their different values tested in our study are detailed in Table 1 for the wide-detector CT and in Table 2 for the dual-source CT. For this latter system, the highest pitch 3.2 was combined with the dual-source mode whereas the other pitch values used the single-source mode. We set the tube voltage at 120 kV and chose a tube current (mA) to deliver an effective tube load as close as possible to the arbitrary target value of 75 mAs for all the acquisition protocols on the two CT systems. The different protocols gave $CTDI_{vol}$ around 5 mGy on the two systems. The transverse slices were reconstructed with a 0.625 mm pixel size (reconstructed FOV 320 mm – matrix 512 x 512) and a slice thickness 1.25 mm for the wide-detector CT and 1.5 mm for the dual-source CT. Reconstruction intervals were half the slice thickness for all the protocols. The reconstruction algorithm and kernel used for all image reconstructions were ASIR-V 50 and STD for the wide-detector CT, Admire 3 and Br40f for the dual-source CT.

### 2.2. In-plane and longitudinal resolution

The sharp edge method described by Samei *et al* [22] was used to measure a 2D in-plane TTF in the circular geometry of the PMMA rod of the phantom in the reconstructed axial slices. On each slice, a square of 120 x 120 $mm^2$ centred on the rod was selected. A radial coordinate positioned at the disc centre was used to divide the disc into angular parts of the same aperture. The PMMA disc was divided into 72 angular portions of 10°, each of them overlapping by 5°. In each angular sector, radial profiles of Hounsfield units (pixel values) originating from the rod center across the edges of the rod gave radial edge spread functions (ESF). The radial ESF for each angular section was generated by rearranging the pixel data according to their distance from the disc centre. The 72 radial ESFs were linearly resampled with a resolution of 10 points per pixel (16 $mm^{-1}$) and Fourier-transformed to give 72 pre-sampling radial TTFs. The 2D in-plane TTF was obtained from the 72 resulting radial TTFs using the angular interpolation method described in Monnin *et al* [23].

The longitudinal resolution ($TTF_z$) of CT slices was determined using the thin wire method described in Gallego Manzano *et al* [24]. A thin

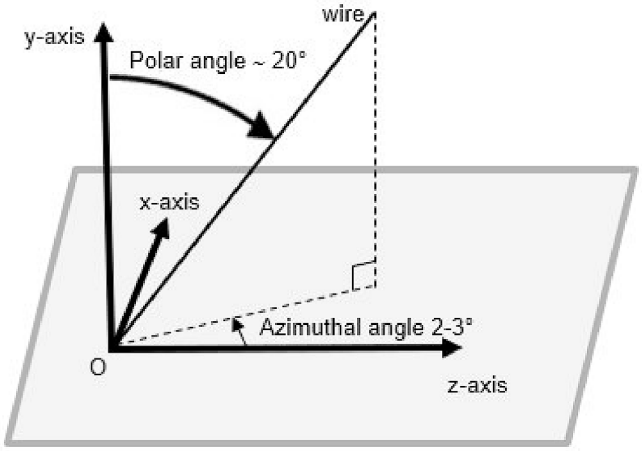


**Fig. 1.** Position of the wire used for the measurement of the longitudinal resolution.

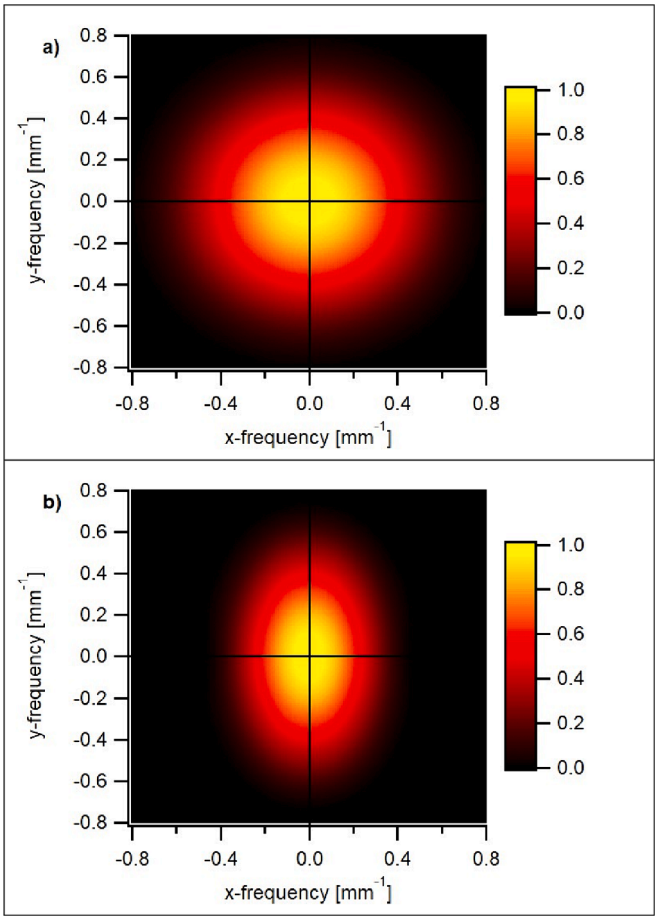


**Fig. 2.** $TTF_{xy}$. a) without motion b) with motion blur along the x-axis.

tungsten wire of diameter 80 μm was stretched vertically in the air, tilted by approximately 20° in the longitudinal z-direction (polar angle), and misaligned by approximately 2-3° in the transverse plane (azimuthal angle) (Fig. 1). The wire diameter equal to 0.128 times the pixel size insured a good oversampling and a negligible influence of the wire on $TTF_z$ measurement. The wire was imaged with the same parameters as the water phantom. The coordinates of the wire position in the slices were determined based on the voxel with the maximum Hounsfield unit (HU) value along the wire direction. The subvoxel wire position in the imaged volume was determined by a linear least squares regression of x-coordinates to y-coordinates of the wire in the transverse slices. The polar angle (inclination) of the wire in a spherical coordinate system was obtained by another linear regression of z-coordinates to azimuthal positions of the wire. The HU values along the linear wire trajectory were plotted relative to the longitudinal wire position to obtain the oversampled longitudinal point spread function (PSF). The longitudinal PSF was linearly resampled over 50 points/voxel to provide the slice sensitivity profile (SSP). The modulus of the discrete Fourier transforms of the SSP normalized to 1.0 at zero frequency gave the longitudinal TTF.

### 2.3. Temporal resolution

During the acquisition, the phantom moved with a uniform rectilinear motion at a controlled speed along the horizontal x-axis in the transverse plane of the scanner. Thus, the rod moving at a constant speed in the image plane generated a 2D spatiotemporal impulse signal whose temporal frequency $f_t = v \cdot f_x$ was proportional to the spatial frequency $f_x$ and speed $v$. The 2D in-plane TTF ($TTF_{xy}$) was at first measured for the PMMA rod moving at a constant speed (Eq. (1)), and then without phantom motion (Eq. (2)).

$$TTF_{xy}(f_x,f_y)\big|_{v>0} = \int_{-\infty}^{\infty} TTF_{xyt}(f_x,f_y,f_t)\,df_t\Big|_{f_t=vf_x} = TTF_{xy}(f_x,f_y)\cdot MTF_t(vf_x) \quad (1)$$

$$TTF_{xy}(f_x,f_y)\big|_{v=0} = TTF_{xy}(f_x,f_y)\cdot MTF_t(0) = TTF_{xy}(f_x,f_y) \quad (2)$$

The static case in Eq. (2) gave the 2D in-plane spatial TTF without motion blur as described in paragraph 2.2 (Fig. 2a). The images resulting from the moving case in Eq. (1) gave the rod blurred and the $TTF_{xy}$ reduced according to the speed of motion in the x-axis (Fig. 2b). The ratio of the TTFs measured with and without phantom motion gave the temporal modulation transfer function ($MTF_t$) expressed in spatial coordinates (Eq. (3)).

$$MTF_t(vf_x) = \frac{TTF_{xy}(f_x,f_y)\big|_{v>0}}{TTF_{xy}(f_x,f_y)\big|_{v=0}} \quad (3)$$

The temporal MTF was rescaled to the temporal frequency coordinate according to Eq. (4).

$$MTF_t(f_t) = MTF_t(vf_x) \quad (4)$$

It is important to note that according to the linear systems theory the temporal MTF is independent of the object type (size and contrast) used for its measurement under the assumption of a small-signal approach, i.e. a small signal perturbation due to a small motion at low speed results in small changes in the output image. The achievement of $MTF_t$ calculation required a careful choice of the phantom speed and a large number of images. The speed of the phantom was chosen to match the frequency bandwidth over which the temporal MTF must be determined. An insufficient speed provides an insufficient temporal bandwidth and an incomplete $MTF_t$ [25] while a too high speed produces motion artifacts that jeopardize the MTF calculation. The phantom displacement on each image was chosen to remain below the pixel size to avoid motion artifacts and was chosen empirically to give a rod displacement of approximately 1/6 of the pixel size per acquisition time by image. The speed was therefore adjusted at approximately between 3 mm/s for the slowest protocols and 46 mm/s for the fastest protocols (Tables 1 and 2). It is also important that the measured TTF is an average over a sufficient number of reconstructed slices. Interpolation artifacts in helical scans depend on the tube angle [26], which is unpredictable, and a reproducible mean effect of the movement on the TTF requires an average over many images. Prior to this study, we evaluated the number of images needed to ensure good reproducibility of TTF. We found that 150 images ensured a good reproducibility with less than 2 % differences between TTFs measured on different images acquired with the same acquisition parameters.

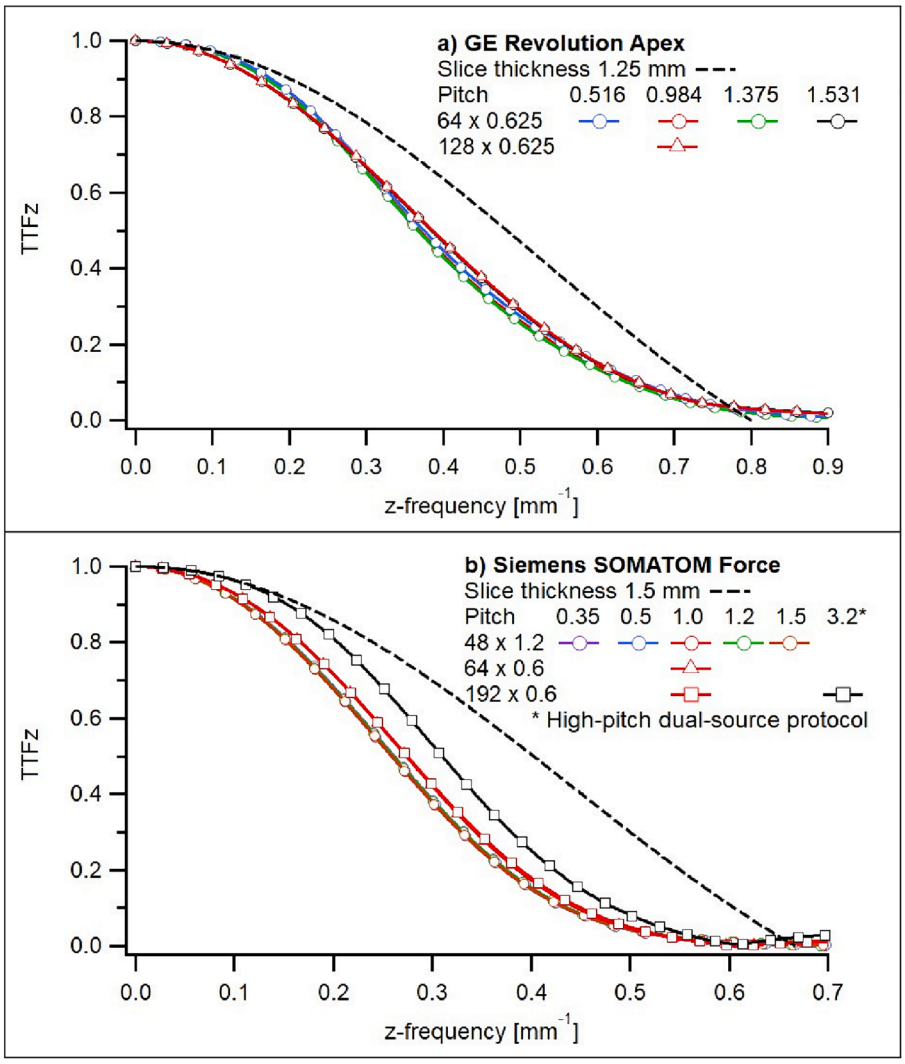


**Fig. 3.** Longitudinal resolution ($TTF_z$).

### 2.4. Noise power spectra (NPS)

Three-dimensional NPS were measured in a homogeneous volume of interest (VOI) of 160 x 160 x 50 $mm^3$ placed at the center of the homogeneous volume of water in the cylindrical phantom. The squared magnitude of the 3D Fourier Transform of pixel values in the VOI gave the 3D NPS, calculated using Eq. (5) [27,28].

$$NPS(f_x,f_y,f_z)=\frac{\Delta x\cdot\Delta y\cdot\Delta z}{N_x\cdot N_y\cdot N_z}\left|\iiint(d(x,y,z)-\bar{d})\cdot\exp\left(-i2\pi(f_x x+f_y y+f_z z)\right)dxdydz\right|^2 \quad (5)$$

Where, d(x,y,z) is the pixel value at the position (x,y,z), $\bar{d}$ is the mean pixel value in the VOI, $N_x$, $N_y$, $N_z$ and $\Delta x$, $\Delta y$, $\Delta z$ are the number of voxels and voxel spacing in the x-, y- and z-directions, respectively. No detrending correction was used to subtract large inhomogeneities from the VOI before NPS calculation. The 2D in-plane NPS were obtained by integrating the 3D NPS along the z-frequency axis. The 1D NPS curves are radial averages of the 2D in-plane NPS, excluding the 0° and 90° axial values, and are expressed is $HU^2mm^2$.

### 2.5. Detectability index

The detectability index $d'$ of a 2 mm diameter PMMA sphere with a contrast ($C_{HU}$) 120 HU (contrast between PMMA and water) was assessed using the non prewhitening with eye filter (NPWE) model observer. The NPWE model has shown good agreement with human observer performance in previous studies on CT images [29,30], and was therefore extended to a spatiotemporal model which includes the object motion blur described by the temporal MTF and the object speed as shown in Eq. (6). We assume the separability between the spatial and temporal components of the spatiotemporal TTF, which are independent because governed by different physical parameters.

$$d'=\frac{C_{HU}\cdot\int_0^{f_{x,Nyq}}\int_0^{f_{y,Nyq}}VTF_{xy}^2(f_x,f_y)\cdot TTF_{xy}^2(f_x,f_y)\cdot MTF_t^2(vf_x)\cdot\left(\int_{-f_{z,Nyq}}^{f_{z,Nyq}}TTF_z(f_z)\cdot S_{obj}(f_x,f_y,f_z)\,df_z\right)^2 df_x df_y}{\sqrt{\int_{-f_{x,Nyq}}^{f_{x,Nyq}}\int_{-f_{y,Nyq}}^{f_{y,Nyq}}VTF_{xy}^4(f_x,f_y)\cdot TTF_{xy}^2(f_x,f_y)\cdot MTF_t^2(vf_x)\cdot\left(\int_{-f_{z,Nyq}}^{f_{z,Nyq}}TTF_z(f_z)\cdot S_{obj}(f_x,f_y,f_z)\,df_z\right)^2\cdot\left(\int_{-f_{t,Nyq}}^{f_{t,Nyq}}NPS(f_x,f_y,f_z)\,df_z\right)df_x df_y}} \quad (6)$$

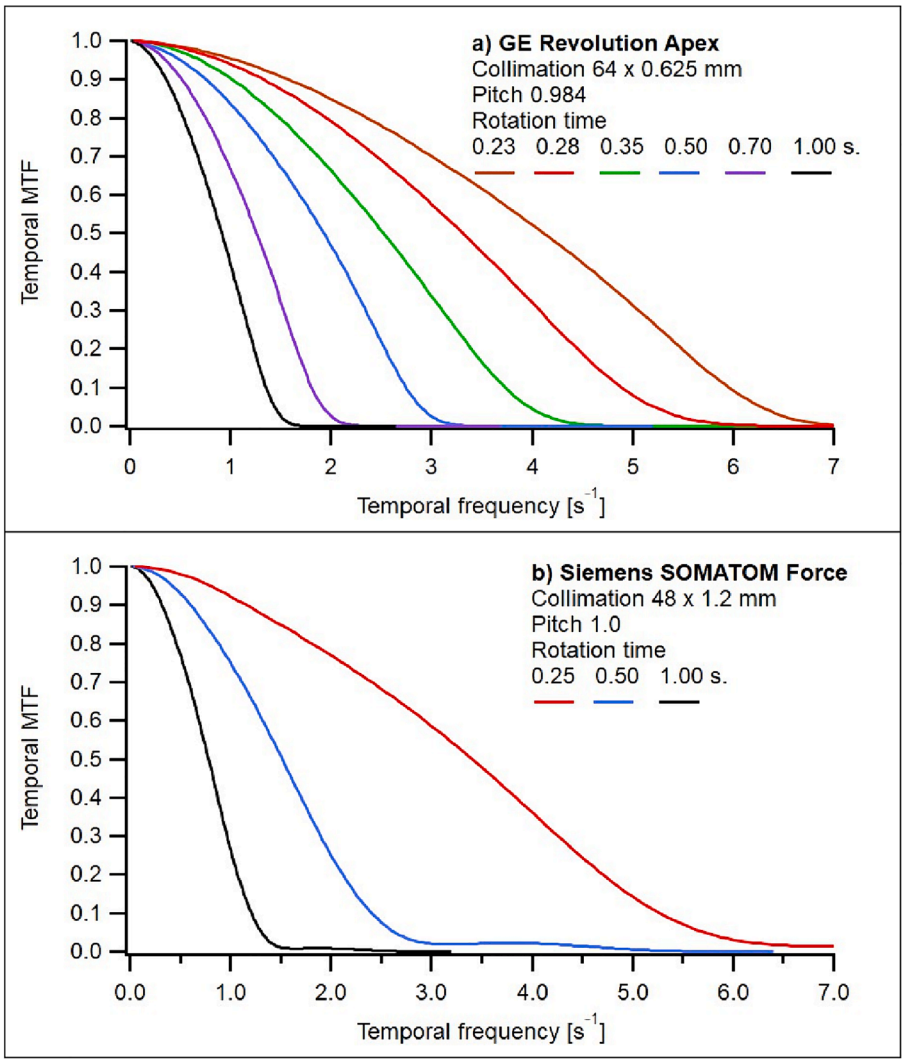


**Fig. 4.** Effect of the rotation time on the temporal MTF.

The observer does not perceive the full volumetric image information of the CT stack of images. The NPWE detectability index was therefore derived in a 2D form pertaining to a single 2D slice extracted from the CT stack. Slice extraction corresponds to an integration of the 3D MTF, NPS and object shape function $S_{obj}$ along the direction orthogonal to the slice, i.e. the z-direction. Therefore, 2D slice metrics were obtained by integrating 3D metrics in the NPWE model. This model only accounts for uniform motions of objects in the image plane and cannot account for nonuniform and/or interslice motions. In Eq. (6), $v$ is the speed of a spherical object of radius $R$ whose shape spectrum ($S_{obj}$) is expressed using a Bessel function of the first kind $J$ in Eq. (7).

$$S_{obj}(f_x,f_y,f_z) = (\sqrt{\pi}R)^3 \cdot \frac{J_{3/2}\left(2\pi R\left(f_x^2+f_y^2+f_z^2\right)^{1/2}\right)}{\left(\pi R\left(f_x^2+f_y^2+f_z^2\right)^{1/2}\right)^{3/2}} \quad (7)$$

The visual transfer function (VTF) represents the contrast sensitivity function of the human eye [31] with a form given in Eq. (8) [32].

$$VTF(f_x,f_y) = \left(f_x^2+f_y^2\right)^{n/2} \cdot \exp\left(-c\left(f_x^2+f_y^2\right)^{a/2}\right) \quad (8)$$

The parameters $n = 1.5$, $c = 3.22$ cycles/° and $a = 0.68$ were used, with a visual distance of 400 mm without display magnification [33,34]. The detectability index was calculated using the measured in-plane TTF, in-plane NPS, longitudinal TTF, and temporal MTF, as a function of the object speed $v$ varying between 0 and 25 mm/s. The maximum speed range (20–25 mm/s) clinically relates to respiratory motion and typical mid-diastolic coronary artery velocity [35].

## 3. Results

### 3.1. In-plane and longitudinal spatial resolution

On the two CT systems, the rotation time, helical pitch and collimation width did not modify the in-plane spatial resolution. The same spatial cutoff frequency at 0.8 mm$^{-1}$ was measured on the two systems. No difference in longitudinal resolution ($TTF_z$) was observed between the ten acquisition protocols tested in our study on the wide-detector system (Fig. 3a). It is interesting to note that pitch factors between 1.0 and 1.531 did not jeopardize the longitudinal resolution. The detector width of 0.6 mm gave slightly higher longitudinal resolution than the detector width of 1.2 mm on the dual-source system (Fig. 3b). Additionally, using the dual-source with the largest pitch 3.2 yielded $TTF_z$ up to 0.12 higher than single-source acquisitions with pitch below or equal to 1.5. The available pitch factors between 0.35 and 1.50 did not modify the longitudinal resolution of single-source protocols.

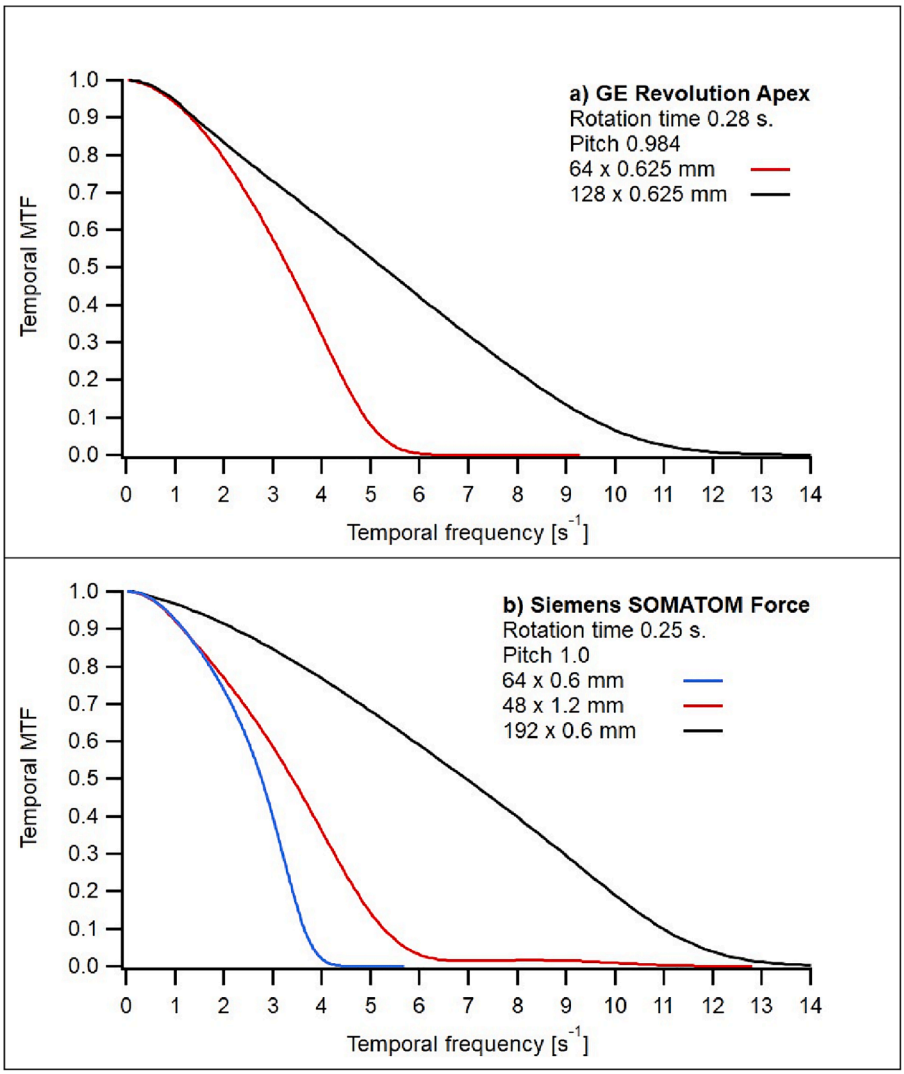


**Fig. 5.** Effect of the collimation width on the temporal MTF.

### 3.2. *Temporal resolution*

The temporal MTF of the two CT systems increased with the tube rotation speed (Fig. 4). For a pitch equal to 0.984, the rotation times of 0.23, 0.28, 0.35, 0.50, 0.70 and 1.0 s. tested on the wide-detector system gave temporal cutoff frequencies of 7.0, 5.7, 4.4, 3.1, 2.2 and 1.6 $s^{-1}$, respectively. This represented a temporal resolution per image between 62 % and 65 % of the rotation time. For a pitch equal to 1.0, the rotation times of 0.25, 0.50 and 1.0 s. tested on the dual-source system gave temporal cutoff frequencies of 6.0, 3.0 and 1.5 $s^{-1}$, respectively, which corresponded to a temporal resolution per image of 67 % the rotation time. Consequently, the temporal cutoff frequency evolved inversely proportional to the gantry rotation time. This result was expected since the acquisition time per image is proportional to the rotation time.

Wider collimations yielded better temporal resolution (Fig. 5). The cutoff frequency of the temporal MTF of the two systems evolved inversely proportional to the collimation width, as expected from the acquisition time per image. For the wide-detector system, with the rotation time 0.28 s and the pitch 0.984, the collimations 40 and 80 mm gave temporal cutoff frequencies at 6.0 and 12.0 $s^{-1}$, respectively. For the dual-source system, the collimations widths 38.4, 57.6 and 115.2 mm gave temporal cutoff frequencies at 4.0, 6.0 and 12.0 $s^{-1}$, respectively, for the pitch 1.0 and the rotation time 0.25 s. The temporal cutoff frequency was found to be proportional to the collimation width.

Increasing the pitch improved the temporal resolution of the two CT systems (Fig. 6). For a rotation time equal to 0.28 s and a collimation of 40 mm, the pitch of 0.516, 0.984, 1.375 and 1.531 tested on the wide-detector system gave temporal cutoff frequencies of 2.2, 6.0, 13.7 and 19.4 $s^{-1}$, respectively. For a rotation time of 0.25 s and the collimation 48 x 1.2 mm, the helical pitch of 0.35, 0.50, 1.0, 1.2 and 1.5 of the dual-source system gave temporal cutoff frequencies of 1.8, 2.3, 6.0, 9.6 and 17.0 $s^{-1}$, respectively. The pitch 3.2 associated to the dual-source acquisition and the wide collimation 192 x 0.6 mm gave the highest temporal cutoff at 23.0 $s^{-1}$. The temporal cutoff frequency increased at a higher rate than the pitch factor, which had a compounding effect on the temporal MTF.

### 3.3. *In-plane noise power spectra (NPS)*

The in-plane NPS (Fig. 7) show a low-frequency increase due to large-scale non-uniformities present in the reconstructed slices. These are mainly due to beam hardening and scattered radiation in the water phantom which produce a trend of HU values from the centre to the periphery. No correction was applied to subtract these large-scale inhomogeneities from the images before NPS calculation. On the wide-detector system, the in-plane NPS demonstrated a variation of up to 20 % in response to changes in pitch and collimation width (Fig. 7a). However, there was no discernible pattern linking the direction of the

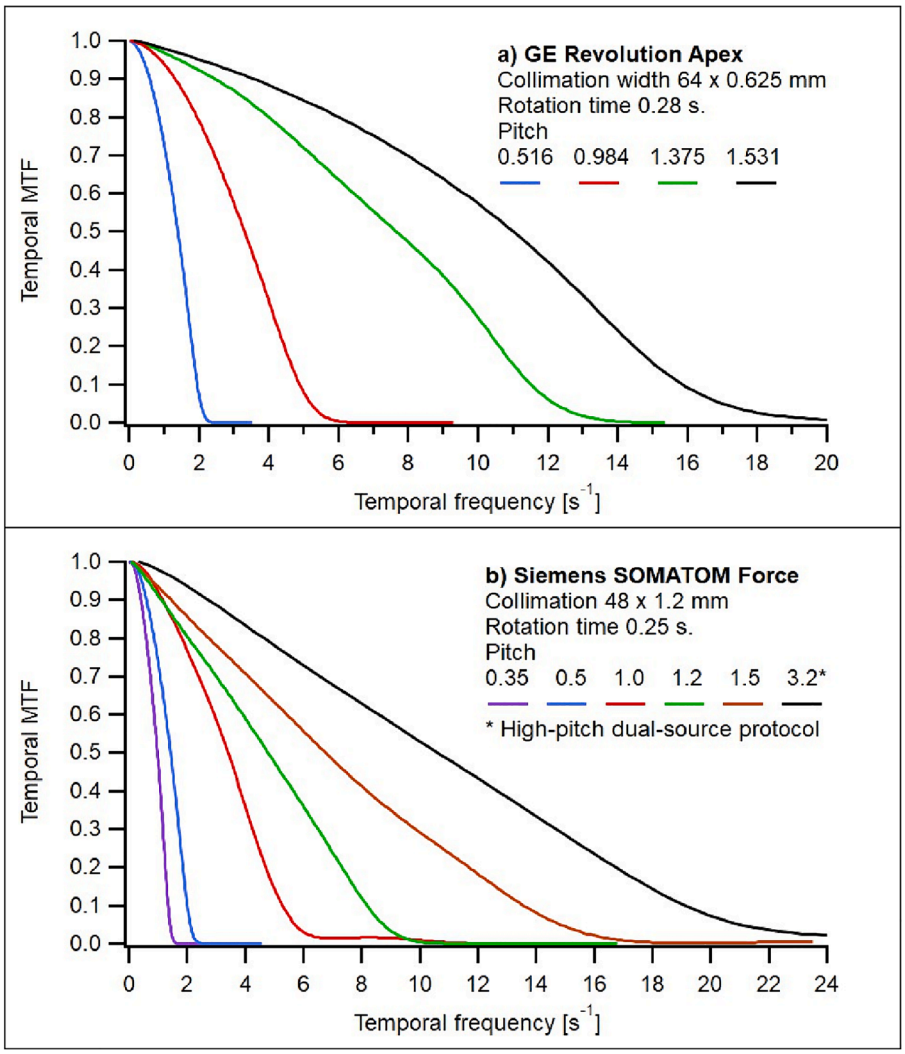


**Fig. 6.** Effect of the helical pitch on the temporal MTF.

variation of these two parameters to the magnitude of the NPS. No difference in NPS was measured as a function of the pitch or collimation width on the dual-source system. Collimations using a detector width 0.6 mm gave a NPS magnitude around 25 % higher than collimations using a detector width 1.2 mm and showed a slight shift of 0.04 $mm^{-1}$ towards low frequencies (Fig. 7b). This difference in in-plane NPS can be explained by changes observed in $NPS_z$ between the two detector widths.

### 3.4. Detectability index

The detectability index *d'* was calculated for a 2 mm diameter PMMA spherical object using the spatiotemporal non-prewhitening with eye filter (NPWE) model observer as a function of the object speed between 0 and 25 mm/s. The object contrast of 120 HU used in the model corresponds to PMMA in water. Increasing the object speed decreased the detectability index. For a static object, the detectability index logically did not depend on the temporal resolution. The detectability reduction was more pronounced at slower rotation times and faster object speeds (Fig. 8). On the dual-source system, an object speed of 20 mm/s typical of a respiratory motion decreased the detectability index by 23.5 %, 43.1 % and 56.9 % for the rotation times 0.25, 0.50 and 1.0 s, respectively. On the wide-detector system, for the same object speed of 20 mm/s, the detectability index decreased only by 14.0 % for the minimal rotation time of 0.23 s, and by 51.2 % for the maximal rotation time of 1.0 s. The largest pitch factors and collimation widths gave the highest detectability indices when the object moved (Fig. 9). On the wide-detector system, the object speed of 20 mm/s decreased the detectability index by 40.4 %, 18.8 %, 7.6 % and 4.9 % for the pitch 0.516, 0.984, 1.375 and 1.531, respectively. On the dual-source system, the detectability index decreased by 50.6 % for the smallest pitch 0.35 and by 9.5 % for the largest pitch 1.5. The protocol using the dual-source with the largest collimation 192 x 0.6 mm associated to the largest pitch 3.2 was the less affected by the increase of the object speed and gave a decrease of only 7.5 % of the detectability index in the same conditions.

## 4. Discussion

High temporal resolution in CT acquisition is crucial to reduce motion blur and improve image quality in many protocols where high temporal resolution is essential to achieve a good diagnosis (thoracic CT, cardiac CT …). The NPWE model has been widely used as a parametric model to assess the task-based detectability on CT images in CT protocol optimization [34,36,37]. The basic model does not take into account the object motion and the temporal performance of CT protocols. The implementation of a NPWE model observer integrating temporal resolution is essential to better assess image quality and benchmark CT protocols where high temporal resolution is mandatory to perform a good diagnosis. The method presented in our study makes it possible to

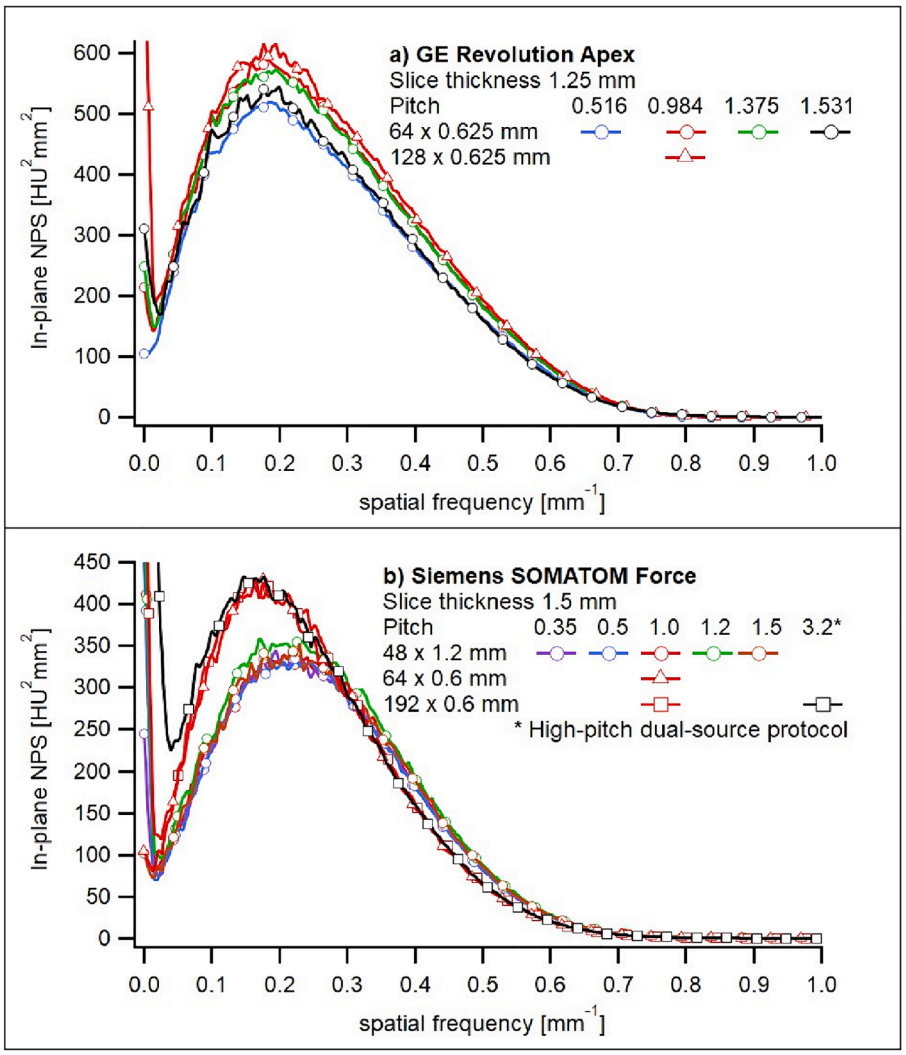


**Fig. 7.** In-plane NPS.

measure the temporal performance of CT protocols at low speeds, compatible with the maximum speed range (20–25 mm/s) linked to respiratory motion and the typical speed of the mid-diastolic coronary artery. The temporal MTF measured using speeds close to clinical conditions was used in a modified formulation of the NPWE model to give a detectability index that provides insight into detectability loss due to motion blur. The NPWE model has shown good agreement with human observer performance in previous studies on CT images [29,30]. Our extension of the NPWE model to a spatiotemporal model which includes the object motion blur is consistent with earlier studies comparing detectability of moving objects in plain images in fluoroscopy [38,39], but has not been compared against human observer performance. Further research is however necessary in order to validate the conditions for which the NPWE model can be used to match the human observer results in the presence of object motion on CT images.

So far, the temporal resolution of CT systems has been mainly characterized in previous studies using the impulse method that produces artifacts that can be difficult to characterize. The assessment of the temporal MTF using uniform linear motion is easier to implement and respects the assumption of the small-signal approach on which the measurement of temporal MTF is based. The validity of the method was tested using variations of basic acquisition parameters (gantry rotation time and collimation width). Good correspondence between theoretical predictions and temporal MTF measurements was achieved for these two parameters. The pitch showed a multiplier effect on the temporal resolution. The calculation of the detectability index gives additional information on how the temporal MTF acts on the detectability of moving objects as a function of their speed. No method comparison could be carried out because no equivalent method for measuring the temporal MTF of CT systems is already in use. The absence of reference results to establish a comparison is a limitation of our study.

The results of the study showed that the temporal resolution of CT scans is controlled by the table speed, managed by the gantry rotation time, the pitch and the collimation width. A higher table speed gives rise to a reduced motion during the acquisition, resulting in less blur and artifacts. As expected, the temporal resolution measured on the moving phantom showed a proportional increase with both the gantry rotation speed and collimation width. Increasing the helical pitch increased the temporal resolution with a multiplier effect observed. A variation in these three parameters did not modify the in-plane resolution and could modify the in-plane NPS up to 25 %. The dual-source protocol gave the highest temporal resolution due to the doubled acquisition rate and the halved acquisition time per image, giving high temporal resolution associated to reduced motion blur [10].

Traditionally, increasing the pitch also leads to a decrease in the longitudinal density of data acquisition, which can negatively affect the slice sensitivity profile [41,42]. However, the decrease in longitudinal resolution for high pitch values was not observed on the two CT systems involved in our study. The slice thickness remained the main parameter that determined the longitudinal resolution. Adaptive axial

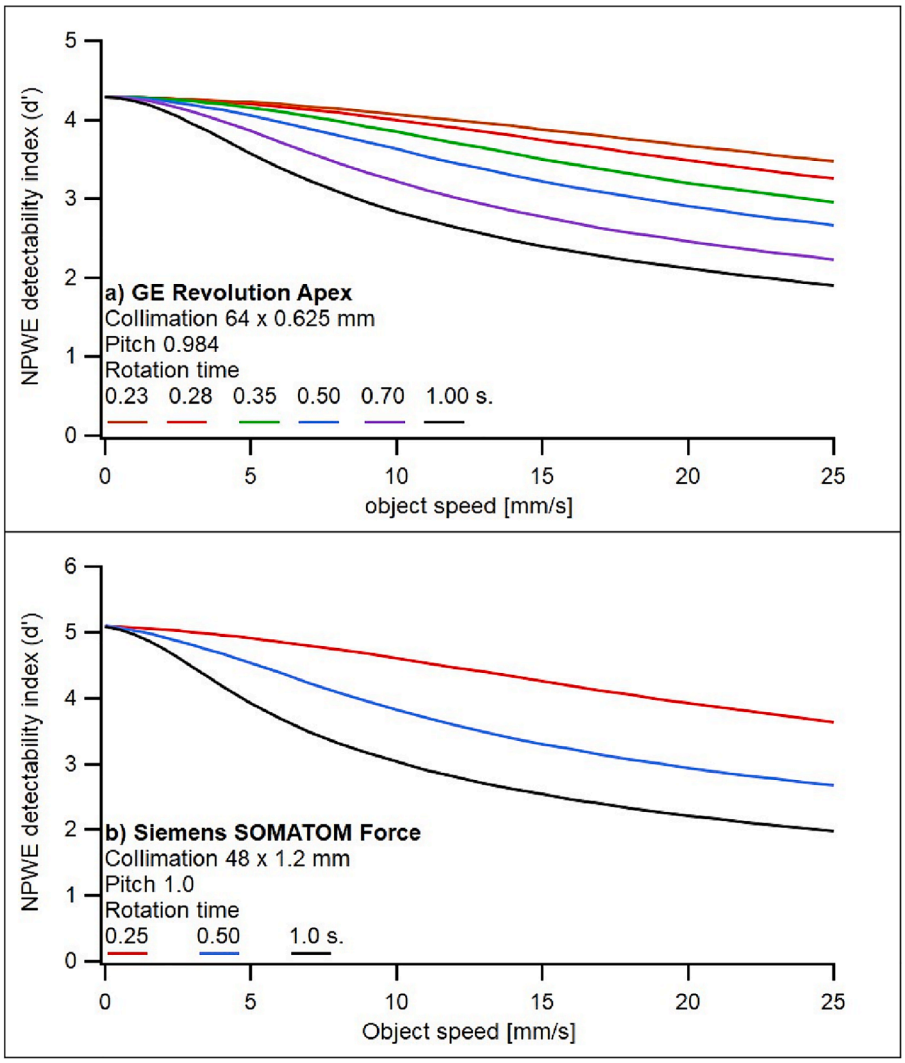


**Fig. 8.** Detectability index of the NPWE observer model as a function of the object speed for different rotation times.

interpolation algorithms combined with wide collimations [43,44,45] and methods for compensation of longitudinal data density such as z-flying focal spot used on the dual-source CT [46] can keep up the longitudinal resolution even for high-pitch scans on recent MDCT. In general, increasing the slice and collimation widths decreases the relative influence of the pitch on the longitudinal resolution. For thinner slices and/or collimations, high pitch values could nevertheless broaden the slice profiles and decrease the z-resolution. Thus, these results cannot be generalized beyond the CT systems, collimations and slices thicknesses studied. In our study, $TTF_z$ solely evaluated the longitudinal resolution without consideration of reconstruction or spiral artifacts which can arise in the longitudinal direction and depend on pitch and data interpolation [47,48]. These elements can be the subject of further investigations. These results showed that recent scanners have overcome the trade-off between temporal and longitudinal resolution.

Using the temporal MTF in Eq. (6) allows the assessment of detectability for any object shape, size and speed. Without temporal MTF, the motion blur should be determined for each object type and speed. The temporal MTF extends the use of the NPWE model to calculate variations in detectability for different object types and speeds. This results in a model that facilitates the optimization of CT protocols for different tasks. As expected, the detectability of moving objects decreased with the motion speed and increased with the temporal resolution. Therefore, fast rotation times, large pitch factors and large collimation widths should be chosen in CT protocols when motion blur can happen. The high-pitch dual-source CT scan provided the best temporal resolution and the highest detectability for moving objects. An increase in rotation speed and pitch factor must be compensated by a higher tube current to maintain the same signal-to-noise ratio (SNR). Higher tube current can require the use of larger focal spot. The compromise between motion and geometric blurs as a function of the rotation time, the motion speed and the focal spot size was not in the scope of our study. This needs to be evaluated specifically for a given scanner and patient size. Regarding the patient exposure, larger collimation widths and higher pitch factors produce a less precise automatic current modulation and wide beam overranging that subjects the patient to unnecessary radiation dose, especially for small helical scan lengths [49]. The adaptive dose shield technology of the dual-source system avoids this deleterious effect by blocking extra doses before and after the spiral scan [50]. On the other hand, the choice of a large collimation width decreases the overbeaming and improves the dose efficiency of the scan. The balance of these two parameters on the patient dose was not measured in our study and must be considered for a particular scanner and scan length in the framework of protocol optimization.

The iterative reconstruction (IR) algorithm and convolution kernel modify the spatial resolution and noise of the reconstructed images but are not expected to have an impact on temporal resolution and therefore on motion blur. The IR algorithms ASIR-V 50 and ADMIRE 3 used in our study have nonlinear characteristics such that the resolution may depend on local noise and image contrast. The TTFs in the xy-plane and

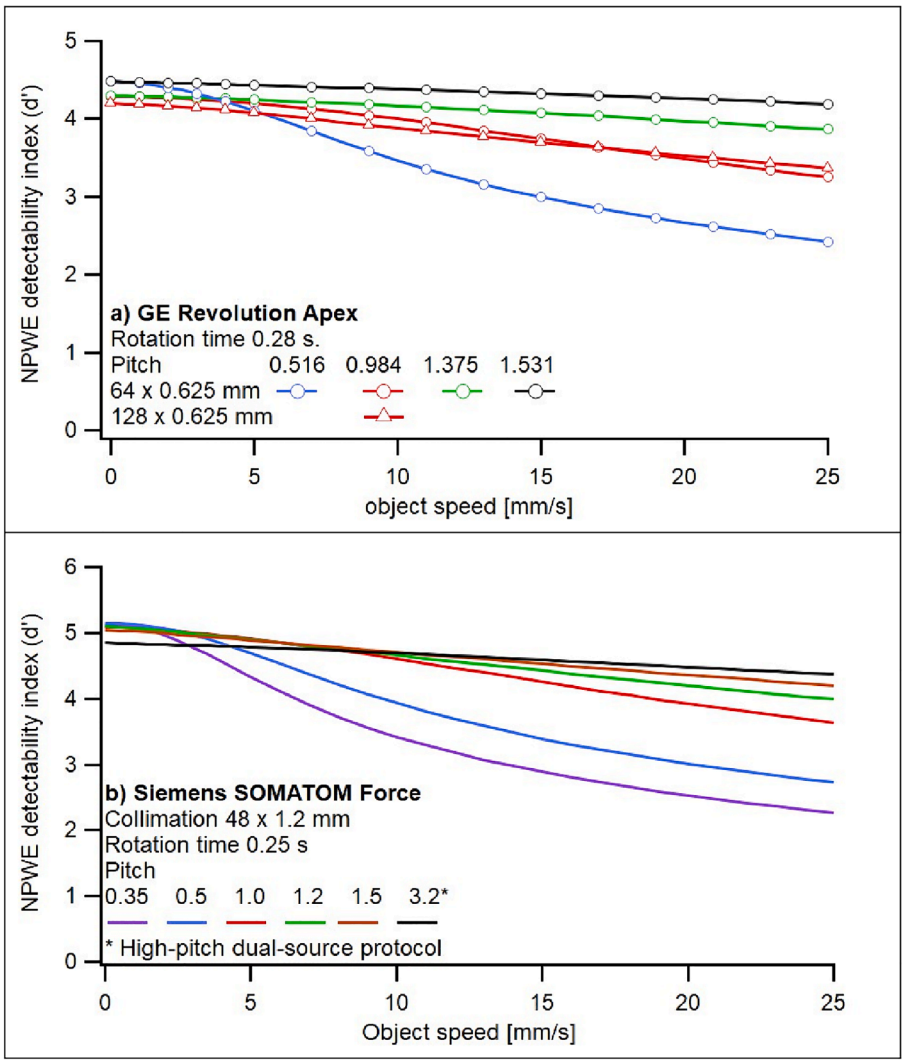


**Fig. 9.** Detectability index of the NPWE observer model as a function of the object speed for different pitch factors and collimation widths.

z-direction were measured using two different objects and methods (PMMA rod in water and thin tungsten wire in air). This difference can therefore produce a variation in resolution which depends on the level of non-linearity of the IR algorithm and impact the accuracy of d' values calculated for an object contrast of 120 HU, different from the contrast around 400 HU given by the tungsten wire. The expected variation in z-resolution due to this difference in contrast should remain small and has been neglected. The reconstruction does not backproject in the z-direction and such a dependence would arise if IR algorithms used "cross-slice" information to reduce in-plane noise, which may arise preferentially with high contrast conditions, highly nonlinear algorithms and thin slice thickness [40]. This would deteriorate the $TTF_z$, which was not observed in our study. The $TTF_z$ are close to their maximal theoretical values determined by the slice thickness (Fig. 3). It is important to keep in mind that linearity and shift-invariance of resolution and noise in the reconstructed volume are only approximations, and Fourier-based metrics use a linear assumption which simplifies the analysis of the actual imaging performance of CT systems and only give an approximation to real performance. A statistical analysis performed in the spatial domain will be more appropriate for the assessment of CT imaging performance in the case of high signal not compatible with the assumption of linearity.

It is important to note that the calculation of the temporal MTF is based on the ratio between two spatial TTFs measured with and without motion. The temporal MTF and NPWE model used in our study only account for uniform rectilinear motions of objects in the image plane and cannot account for a loss of detectability due to an interslice and/or nonuniform motion. If organs or lesions motions in the abdomen or pelvis are in general greater in the head-feet (HF) direction, the amplitude of motion may be as high as 5.0 mm and 3.0 mm in the antero-posterior and mediolateral directions, respectively [51,52]. The out-of-plane HF motion component creates peculiar artifacts and a blur component reduced by projection onto the image plane. A comprehensive 3D assessment of temporal MTF and motion blur should be investigated to understand three-dimensional object motions. It was beyond the scope of this study. Our measurement method is based on the linear systems theory and on the assumption that small changes in the input lead to small changes in the output image. The object motion speed must be small enough to produce small variations in the images, i.e. only blur. High object speed would produce (nonlinear) artifacts that could not be characterized using our method. This is a limitation of our method which is restrained to blur characterization and excludes the characterization of motion artifacts. Fourier-based metrics give a simplified linear analysis of CT systems and only give a good estimate of actual performance in terms of spatial resolution, noise and also temporal resolution. Nevertheless, the temporal resolution measured using the moving phantom showed a proportional increase with both the gantry rotation speed and collimation width. These results indicate the output blur signal was a direct, linear (proportional) function to these two acquisition parameters for the range of motion speeds tested in our

study. Our choices must be understood as limitations in accuracy and future work should therefore be conducted in more realistic settings to consider all the complexity of volume and nonlinear object motions.

## 5. Conclusion

This work introduced and systematically assessed a new method for evaluating the temporal resolution of CT protocols. As figure of merit the detectability index in a NPWE model observer was extended to characterize the temporal performance of CT protocols. It could quantify the deleterious effect of motion blur on detection performance as a function of object speed and showed the importance of considering temporal resolution when attempting to characterize the detection performance of the imaging protocols. On the two modern CT systems tested in our study, a faster rotation speed, a higher helical pitch or larger collimation width all improved the temporal resolution without jeopardizing the in-plane resolution and noise nor the longitudinal resolution. However, special attention should be paid to overbeaming when using large pitch factors and collimations for short scan lengths. The consideration of these elements associated to the method proposed in this study can be used for benchmarking CT protocols which require high image quality and high temporal resolution.

## Declaration of competing interest

The authors declare that they have no known competing financial interests or personal relationships that could have appeared to influence the work reported in this paper.

## References


[1] Kalisz K, Buethe J, Saboo SS, Abbara S, Halliburton S, Rajiah P. Artifacts at cardiac CT: physics and solutions. Radiographics 2016;36:2064–83. https://doi.org/10.1148/rg.2016160079.

[2] Zhang Q, Hu Y-C, Liu F, Goodman K, Rosenzweig KE, Mageras GS. Correction of motion artifacts in cone-beam CT using a patient-specific respiratory motion model. Med Phys 2010;37:2901–12299. https://doi.org/10.1118/1.3397460.

[3] Mahesh M, Cody DD. Physics of cardiac imaging with multiple-row detector CT. Radiographics 2007;27:1495–509. https://doi.org/10.1148/rg.275075045.

[4] Shin JH, Lee HK, Choi CG, Suh DC, Lim T-H, Kang W. The quality of reconstructed 3D images in multidetector-row helical CT: Experimental study involving scan Parameters. Korean J Radiol 2002;3:49–56. https://doi.org/10.3348/kjr.2002.3.1.49.

[5] Sahani D, Saini S, D'Souza RV, O'Neill MJ, Prasad SR, Kalra MK, et al. Comparison between low (3:1) and high (6:1) pitch for routine abdominal/pelvic imaging with multislice computed tomography. J Comput Assist Tomogr 2003;27:105–9. https://doi.org/10.1097/00004728-200303000-00001.

[6] Achenbach S, Marwan M, Schepis T, Pflederer T, Bruder H, Allmendinger T, et al. High-pitch spiral acquisition: a new scan mode for coronary CT angiography. J Cardiovasc Comput Tomogr 2009;3:117–21. https://doi.org/10.1016/j.jcct.2009.02.008.

[7] Lell MM, May M, Deak P, Alibek S, Kuefner M, Kuettner A, et al. High-pitch spiral computed tomography: effect on image quality and radiation dose in pediatric chest computed tomography. Invest Radiol 2011;46:116–23. https://doi.org/10.1097/rli.0b013e3181f33b1d.

[8] Tang J, Hsieh J, Guang-Hong C. Temporal resolution improvement in cardiac CT using PICCS (TRI-PICCS): performance studies. Med Phys 2010;37:4377–87. https://doi.org/10.1118/1.3460318.

[9] Flohr TG, Leng S, Yu L, Allmendinger T, Bruder S, Petersilka M, et al. Dual-source spiral CT with pitch up to 3.2 and 75 ms temporal resolution: image reconstruction and assessment of image quality. Med Phys 2009;36:5641–53. https://doi.org/10.1118/1.3259739.

[10] Schmidt B, Flohr T. Principles and applications of dual source CT. Phys Med 2020;79:36–46. https://doi.org/10.1016/j.ejmp.2020.10.014.

[11] Hou DJ, Tso DK, Davison C, Inacio J, Louis LJ, Nicolaou S, et al. Clinical utility of ultra high pitch dual source thoracic CT imaging of acute pulmonary embolism in the emergency department: are we one step closer towards a non-gated triple rule out? Eur J Radiol 2013;82:1793–8. https://doi.org/10.1016/j.ejrad.2013.05.003.

[12] Kawashima H, Ichikawa K, Takata T, Nagata H, Hoshika M, Akagi N. Technical note: performance comparison of ultra-high-resolution scan modes of two clinical computed tomography systems. Med Phys 2020;47:488–97. https://doi.org/10.1002/mp.13949.

[13] Taguchi K, Anno K. High temporal resolution for multislice helical computed tomography. Med Phys 2000;27:861–72. https://doi.org/10.1118/1.598951.

[14] McCollough CH, Schmidt B, Yu L, Primak A, Ulzheimer S, Bruder S, et al. Measurement of temporal resolution in dual source CT. Med Phys 2008;35:764–8. https://doi.org/10.1118/1.2826559.

[15] Ichikawa K, Hara T, Urikura A, Takata T, Ohashi K. Assessment of temporal resolution of multi-detector row computed tomography in helical acquisition mode using the impulse method. Phys Med 2015;31:374–81. https://doi.org/10.1016/j.ejmp.2015.02.012.

[16] Hara T, Urikura A, Ichikawa K, Hoshino T, Nishimaru E, Niwa S. Temporal resolution measurement of 128-slice dual source and 320-row area detector computed tomography scanners in helical acquisition mode using the impulse method. Phys Med 2016;32:625–30. https://doi.org/10.1016/j.ejmp.2016.02.015.

[17] Ertel D, Kröber E, Kyriakou Y, Langner O, Kalender WA. Modulation transfer function – based assessment of temporal resolution: validation for single- and dual-source CT. Radiology 2008;248:1013–7. https://doi.org/10.1148/radiol.2482072173.

[18] Saito H, Ito T, Tsujiguchi T, Yamaguchi M, Kashiwakura I. Characteristics of temporal resolutionin 16- and 64-row computed tomography scanners. Radiol Phys Technol 2018;11:100–8. https://doi.org/10.1007/s12194-017-0436-z.

[19] Richard S, Husarik DB, Yadava G, Murphy SN, Samei E. Towards task-based assessment of CT performance: system and object MTF across different reconstruction algorithms. Med Phys 2012;39:4115–22. https://doi.org/10.1118/1.4725171.

[20] Verdun FR, Racine D, Ott JG, Tapiovaara MJ, Toroi P, Bochud FO, et al. Image quality in CT: from physical measurements to model observers. Phys Med 2015;31:823–43. https://doi.org/10.1016/j.ejmp.2015.08.007.

[21] Rotzinger DC, Racine D, Beigelman-Aubry C, Alfudhili KM, Keller N, Monnin P, et al. Task-based model observer assessment of a partial model-based iterative reconstruction algorithm in thoracic oncologic multidetector CT. Sci Rep 2018;8:1–12. https://doi.org/10.1038/s41598-018-36045-4.

[22] Samei E, Flynn MJ, Reimann DA. A method for measuring the presampled MTF in digital radiographic systems using an edge test device. Med Phys 1998;25:102–13. https://doi.org/10.1118/1.598165.

[23] Monnin P, Bosmans H, Verdun FR, Marshall NW. A comprehensive model for quantum noise characterization in digital mammography. Phys Med Biol 2016;61:2083–108. https://doi.org/10.1088/0031-9155/61/5/2083.

[24] Gallego Manzano L, Monnin P, Sayous Y, Becce F, Damet J, Viry A. Clinical commissioning of the first point-of-care spectral photon-counting CT for the upper extremities. Med Phys 2023;38:1–16. https://doi.org/10.1002/mp.16313.

[25] Monnin P, Viry A, Damet J, Nowak M, Vitzthum V, Racine D. A novel method to assess the spatiotemporal image quality in fluoroscopy. Phys Med Biol 2021;66:245001. https://doi.org/10.1088/1361-6560/ac3c15.

[26] Van Straten M, Venema HW, Hartman J, den Heeten GJ, Grimbergen CA. Reproducibility of multi-slice spiral computed tomography scans: an experimental study. Med Phys 2004;31:2785–6. https://doi.org/10.1118/1.1796131.

[27] Dobbins JT, Samei E, Ranger NT, Chen Y. Intercomparison of methods for image quality characterization. II Noise power spectrum Med Phys 2006;33:1466–75. https://doi.org/10.1118/1.2188819.

[28] Boedeker KL, Cooper VN, McNitt-Gray MF. Application of the noise power spectrum in modern diagnostic MDCT: part I. measurement of noise power spectra and noise equivalent quanta. Phys Med Biol 2007;52:4027–46. https://doi.org/10.1088/0031-9155/52/14/002.

[29] Gang GJ, Lee J, Stayman JW, Tward DJ, Zbijewski W, Prince JL, et al. Analysis of fourier-domain task-based detectability index in tomosynthesis and cone-beam CT in relation to human observer performance. Med Phys 2011;38:1754–68. https://doi.org/10.1118/1.3560428.

[30] Gang GJ, Stayman JW, Zbijewski W, Siewerdsen JH. Task-based detectability in CT image reconstruction by filtered backprojection and penalized likelihood estimation. Med Phys 2014;41. https://doi.org/10.1118/1.4883816. 081902–1-19.

[31] Barten PGJ. Evaluation of subjective image quality with the square-root integral method. J Opt Soc Am A 1990;7:2024–31. https://doi.org/10.1016/j.zemedi.2021.01.004.

[32] Burgess AE. Statistically defined backgrounds: performance of a modified nonprewhitening observer model. J Opt Soc Am A 1994;11:1237–42. https://doi.org/10.1364/josaa.11.001237.

[33] Saunders RS, Samei E. Resolution and noise measurements of five CRT and LCD medical displays. Med Phys 2006;33:308–19. https://doi.org/10.1118/1.2150777.

[34] Solomon J, Samei E. Correlation between human detection accuracy and observer model-based image quality metrics in computed tomography. J Med Imaging 2016;3:035506. https://doi.org/10.1117/1.JMI.3.3.035506.

[35] Husmann L, Leschka S, Desbiolles S, Schepis T, Gaemperli O, Seifert B, et al. Coronary artery motion and Cardiac phases: dependency on Heart rate – implications for CT image reconstruction. Radiology 2007;245:567–76. https://doi.org/10.1148/radiol.2451061791.

[36] Viry A, Aberle C, Lima T, Treifer R, Schindera ST, Verdun FR, et al. Assessement of task-based image quality for abdominal CT protocols linked with national diagnostic reference levels. Eur Radiol 2021;32:1227–37. https://doi.org/10.1007/s00330-021-08185-1.

[37] Othman N, Simon A-C, Montagu T, Berteloot L, Grévent D, Geryes BH, et al. Toward a comparison and an optimization of CT protocols using new metrics of dose and image quality part I: prediction of human observers using a model observer for detection and discrimination tasks in low-dose CT images in various scanning conditions. Phys Med Biol 2021;66:115003. https://doi.org/10.1088/1361-6560/abfad8.

[38] Xue P, Wilson DL. Detection of moving objects in pulsed-x-ray fluoroscopy. J Opt Soc Am A 1998;15:375–88. https://doi.org/10.1364/josaa.15.000375.

[39] Wilson DL, Jabri KN, Aufrichtig R. Perception of temporally filtered X-ray fluoroscopy images. IEEE Trans Med Imaging 1999;18:22–31. https://doi.org/10.1109/42.750250.

[40] Chen B, Christianson O, Wilson JM, Samei E. Assessment of volumetric noise and resolution performance for linear and nonlinear CT reconstruction methods. Med Phys 2014;41. https://doi.org/10.1118/1.4881519. 071909–1-12.
[41] Crawford CR, King KF. Computed tomography scanning with simultaneous patient translation. Med Phys 1990;17:967–82. https://doi.org/10.1118/1.596464.
[42] Hu H, Fox SH. The effect of helical pitch and beam collimation on the lesion contrast and slice profile in helical CT imaging. Med Phys 1996;23:1943–54. https://doi.org/10.1118/1.597774.
[43] Klingenbeck-Regn K, Schaller S, Flohr T, Ohnesorge B, Kopp AF, Baum U. Subsecond multi-slice computed tomography: basics and applications. Eur J Radiol 1999;31:110–24. https://doi.org/10.1016/S0720-048X(99)00086-8.
[44] Schaller S, Flohr T, Klingenbeck K, Krause J, Fuchs T, Kalender WA. Spiral interpolation algorithm for multislice spiral CT – Part I: theory. IEEE Trans Med Imaging 2000;19:822–34. https://doi.org/10.1109/42.887832.
[45] Fuchs T, Krause J, Schaller S, Flohr T, Kalender WA. Spiral interpolation algorithm for multislice spiral CT – Part II: measurement and evaluation of slice sensitivity profiles and noise at a clinical multislice system. IEEE Trans Med Imaging 2000;19:835–47. https://doi.org/10.1109/42.887833.
[46] Flohr TG, Stierstorfer K, Ulzeihmer S, Bruder S, Primak AN, McCollough CH. Image reconstruction and image quality evaluation for a 64-slice CT scanner with z-flying focal spot. Med Phys 2005;32:2536–47. https://doi.org/10.1118/1.1949787.
[47] La Rivière PJ, Pan X. Pitch dependence of longitudinal sampling and aliasing effects in multi-slice helical computed tomography (CT). Phys Med Biol 2002;47:2797–810. https://doi.org/10.1088/0031-9155/47/15/318.
[48] Bricault I, Ferretti G. A general tool for the evaluation of spiral CT interpolation algorithms: revisiting the effect of pitch in multislice CT. IEEE Trans Med Imaging 2005;24:58–69. https://doi.org/10.1109/tmi.2004.837793.
[49] Merzan D, Nowik P, Poludniowski G, Bujila R. Evaluating the impact of scan settings on automatic tube current modulation in CT using a novel phantom. Br J Radiol 2017;90:20160308. https://doi.org/10.1259/bjr.20160308.
[50] Yang K, Li Z, Li X, Liu B. Characterization of dynamic collimation mechanisms for helical CT scans with direct measurements. Phys Med Biol 2019;64:215006. https://doi.org/10.1088/1361-6560/ab3eaa.
[51] Keall PJ, Mageras GS, Balter JM, Emery RS, Forster KM, Jiang SB, et al. The management of respiratory motion in radiation oncology report of AAPM task group 76. Med Phys 2006;33:3874–900. https://doi.org/10.1118/1.2349696.
[52] Yoganathan SA, Maria Dias KJ, Agarwal A, Kumar S. Magnitude, impact and management of respiration-induced target motion in radiotherapy treatment: a comprehensive review. J Med Phys 2017;42:101–15. https://doi.org/10.4103/jmp.JMP_22_17.